Snowflake phononic topological insulator at the nanoscale

Christian Brendel

Max Planck Institute for the Science of Light, Staudtstraße 2, 91058 Erlangen, Germany

Vittorio Peano

Department of Physics, University of Malta, Msida MSD 2080, Malta

Oskar Painter

Institute for Quantum Information and Matter and Thomas J. Watson, Sr. Laboratory of Applied Physics,
California Institute of Technology, Pasadena, California 91125, USA

Florian Marquardt

Max Planck Institute for the Science of Light, Staudtstraße 2, 91058 Erlangen, Germany
and Institute for Theoretical Physics, University of Erlangen-Nürnberg, Staudtstraße 7, 91058 Erlangen, Germany

We show how the snowflake phononic crystal structure, which recently has been realized experimentally, can be turned into a topological insulator for mechanical waves. This idea, based purely on simple geometrical modifications, could be readily implemented on the nanoscale.

Introduction. The first examples of topologically protected mechanical wave transport have just emerged during the past three years. So far, experimental implementations exist on the centimeter scale, both for the case of time-reversal symmetry broken by external driving [1], such as in coupled gyroscopes, as well as for the case without driving [2–6], such as in coupled pendula. Moreover, a multitude of different implementations have been envisioned theoretically [7–24]. However, it is highly desirable to come up with alternative design ideas that may be realized on the nanoscale, eventually pushing towards applications in integrated phononics. The first theoretical proposal of this kind [25] suggested to exploit the optomechanical interaction to generate *chiral* (unidirectional) mechanical waves in a phononic crystal. While that approach is particularly robust against disorder, it requires breaking the time-reversal symmetry by an external laser drive. To avoid this requirement, one can resort to topological insulators, with *helical* mechanical waves where the propagation direction depends on a (pseudo)spin. These can be implemented using a purely geometrical approach. A first step in this direction is the phononic crystal design proposed in Ref. [26]. However, it requires feature sizes much smaller than the phonon wavelength. It is thus impossible to reach wavelengths comparable to the smallest feature sizes allowed by nanofabrication. In this Rapid Communication, we propose a simple modification to an already existing structure, the so-called snowflake phononic crystal, that has already proven to be a reliable platform for nanoscale optomechanics [27], and could also support pseudomagnetic fields for mechanical waves [28]. With the proposed modification, which is inspired by an idea first analyzed by Wu and Hu for photonic systems [29] (see also Ref. [30] for the corresponding experimental implementation and Refs. [17,18,23,31] for related theoretical work), we are

able to create a topological insulator for mechanical waves based on a proven nanoscale platform.

Original snowflake design. The snowflake crystal is a planar quasi-two-dimensional crystal slab patterned with snowflake-shaped holes arranged on a triangular lattice. Thus, it exhibits $\mathcal{D}_{6h}$ symmetry (sixfold rotational symmetry with in-plane and out-of-plane reflections). Strictly speaking, it is an optomechanical crystal, but here we will only make use of its phononic properties which we investigate by solving the full elasticity equations [32,33], as well as approximate analytical treatments and tight-binding models. The phononic crystal band structure is shown in Fig. 1(c). It displays Dirac cones at the two high-symmetry points, **K** and **K**′. The geometrical parameters are optimized to obtain spectrally well isolated Dirac cones in view of opening a complete topological band gap for the modified crystal, as described below.

Topological design. The proposed modification consists in changing the radius of every third snowflake [cf. Fig. 1(a)]. By doing so, we break the original translational symmetry while preserving the point group. The new Wigner-Seitz cell, with a single modified snowflake at its center, is enlarged by a factor of 3, while the Brillouin zone (BZ) is reduced by the same factor [cf. Fig. 1(b)]. We anticipate this reduction by folding the band structure for the as-yet unperturbed structure into the new BZ [see Figs. 1(a) and 1(b)]. This maps the Dirac cones from **K** and **K**′ points of the old BZ to the **Γ** point of the new BZ, forming a degenerate pair of Dirac cones at **Γ** [Figs. 1(c) and 1(d)]. For the new structure, the breaking of the translational symmetry of the original structure splits the cones, opening a complete band gap [Fig. 1(e)]. Below, we show that such a band gap can be topological in nature.

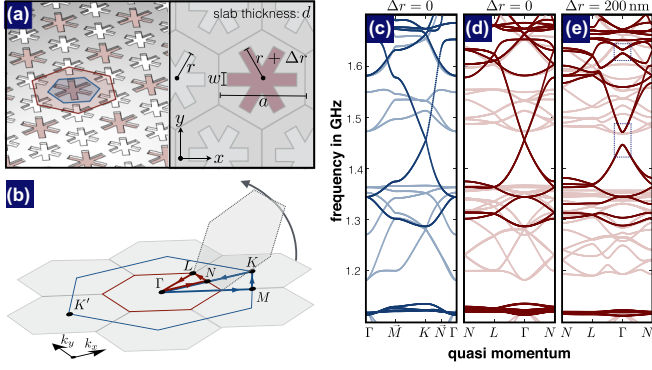*Effective Hamiltonian.* We complement our finite-element method (FEM) simulations by deriving an effective

FIG. 1. Setup and bulk band structures (FEM simulations). (a) Snowflake crystal design defined by the parameters $(a, r, w, d, \Delta r)$, where d is the slab thickness. For $\Delta r = 0$ ($\Delta r \neq 0$), the border of the Wigner-Seitz cell is drawn in blue (red). (b) Reciprocal space. The edges of the corresponding Brillouin zones are drawn in the same colors. Also plotted are the contours along which the band structures in (c) (blue contours) and (d) and (e) (red contours) are calculated. (c) Band structure for $\Delta r = 0$. (d) Same band structure, but folded into the smaller BZ. The Dirac cones at the **K** and **K′** points are now mapped onto the **Γ** point. (e) Band structure for $\Delta r \neq 0$. The Dirac cones are now gapped. Note that the same behavior is observed for several Dirac cones (highlighted by dotted boxes). The modes symmetric to the xy plane are displayed in darker colors. [Here, we have considered a silicon crystal slab with a Young's modulus of 170 GPa, mass density 2329 kg/m³, Poisson's ratio 0.28, and geometrical parameters $(a, r, w, d) = (5000, 1800, 750, 220)$ nm.]

Hamiltonian valid for long wavelengths. In this context, the normal mode wave function $\boldsymbol{\psi}(x, y, z)$ is a complex three-dimensional vector field related to the mechanical displacement field $\mathbf{u}(x, y, z)$ by $\mathbf{u} = \mathrm{Re}[\boldsymbol{\psi} \cdot e^{-i\omega t}]$, where ω is the normal mode eigenfrequency. We follow a route that clarifies the connection to the original valley degree of freedom. The results can alternatively be explained by the symmetry arguments first advocated for $\mathcal{C}_6$-symmetric structures in a photonic context in Ref. [29]. We start by pointing out that the Dirac cones of the regular snowflake crystal stem from an essential degeneracy enforced by the $\mathcal{C}_{6v}$ symmetry. Such a degeneracy occurs whenever a normal mode $|\psi_{\sigma,\tau}\rangle$ has threefold quasiangular momentum $\sigma = +1$ or $\sigma = -1$ for quasimomentum **K** (corresponding to $\tau = 1$) or **K′** (corresponding to $\tau = -1$). That this indeed occurs for the tip of a cone can be verified using finite-element simulations (see Ref. [28], where the mode displacement fields are shown for similar parameters). By applying the symmetries $\hat{M}_{xz}$ (reflection through the plane xz), and $\hat{R}_\pi$ (180° rotation) it follows that the state belongs to a quadruplet of degenerate states $|\psi_{\sigma,\tau}\rangle$ ($\sigma = \pm 1$ and $\tau = \pm 1$) fulfilling

$$|\psi_{\sigma,\tau}\rangle = \hat{M}_{xz}|\psi_{-\sigma,\tau}\rangle = \hat{R}_\pi|\psi_{\sigma,-\tau}\rangle. \quad (1)$$

Next, we introduce two sets of Pauli matrices to span this four-dimensional Hilbert space. One set encodes the valley degree of freedom $\hat{\tau}_{\{x,y,z\}}$ and another one the quasiangular degree of freedom $\hat{\sigma}_{\{x,y,z\}}$, such that $\hat{\tau}_z|\psi_{\sigma,\tau}\rangle = \tau|\psi_{\sigma,\tau}\rangle$ and $\hat{\sigma}_z|\psi_{\sigma,\tau}\rangle = \sigma|\psi_{\sigma,\tau}\rangle$, and the usual set of Pauli matrices holds in this basis.

We now write the Hamiltonian as a Taylor series up to linear order in $\mathbf{k}$ by using the above matrices. By keeping only terms that are invariant under the time-reversal symmetry $\hat{T}$, 60°
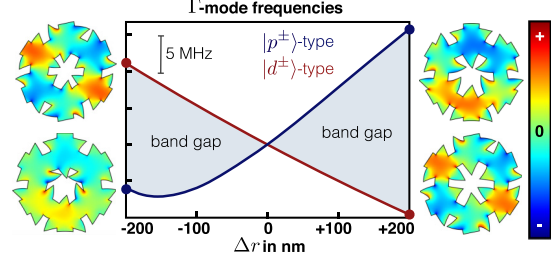
rotations $\hat{R}_{\pi/3}$, and $\hat{M}_{xz}$, we obtain [33]

$$\hat{H}_\mathbf{k} = g\hat{\tau}_x + v\hat{\tau}_z(k_x\hat{\sigma}_x - k_y\hat{\sigma}_y). \quad (2)$$

This derivation can be generalized to systems without the symmetry $\hat{M}_{xz}$ (in-plane point group $\mathcal{C}_6$) [see Supplemental Material (SM) [33]]. Up to a unitary transformation, Hamiltonian (2) is the large-wavelength limit of the Bernevig-Hughes-Zhang model for a topological insulator [34]. Here, the conserved helicity is the matrix $\hat{S} = \hat{\tau}_x\hat{\sigma}_z$. Combined with the time-reversal operator, it gives rise to a pseudo-time-reversal symmetry $(\hat{T}\hat{S})$, which squares to minus the identity, directly leading to Kramer's degeneracy. The first term in Eq. (2) is induced by the breaking of the translational symmetry of the original structure and is responsible for gapping the Dirac cones. In other words, g can be interpreted as a mass. At the Γ point, the common eigenstates of $\hat{H}_{\mathbf{k}=0}$ and $\hat{S}$ are the states $|p^\pm\rangle$ and $|d^\pm\rangle$ which obey $\hat{\tau}_x|d^\pm\rangle = |d^\pm\rangle$, $\hat{\tau}_x|p^\pm\rangle = -|p^\pm\rangle$, $\hat{S}|p^\pm\rangle = \mp|p^\pm\rangle$, and $\hat{S}|d^\pm\rangle = \mp|d^\pm\rangle$. One can show that these states are actually of p and d type with respect to 60° rotations [33]

$$\hat{R}_{\pi/3}|p^\pm\rangle = e^{\pm i\pi/3}|p^\pm\rangle, \quad \hat{R}_{\pi/3}|d^\pm\rangle = e^{\pm i2\pi/3}|d^\pm\rangle.$$

Thus, the band inversion signaling a topological phase is realized for $g < 0$. Note that away from the Γ point only states of the same helicity ($s = \pm 1$) will get mixed to form the finite-k eigenstates. This conservation law emerges because the terms which are linear in $\mathbf{k}$ can induce transitions only between states whose 60° quasiangular momenta differ by one quantum: p^+ to d^+ and p^- to d^- [33]. Higher-order terms (e.g., $\sim k^2$) not included in Eq. (2) mix different helicities [33] but are negligible close to the Γ point. An indirect signature of this coupling is the lifting of the degeneracy of the two helicities. Remarkably, for our specific design, the splitting remains smaller than 1.5% of the band gap even for a quasimomentum as large as 1/4 of the distance to the boundary of the Brillouin zone, $|\mathbf{k}| \leqslant \pi/(6a)$.

From Eq. (2), we see that the snowflake crystal undergoes a topological phase transition whenever the mass g changes sign. We can simply tune g by varying the radius of the central snowflake (see Fig. 2). The behavior of g can be understood by noting that the p orbitals have extra nodes at the external links leading out of the (enlarged) unit cell (enforced by a phase

FIG. 2. Band inversion (FEM simulations): Frequencies of the $|p^\pm\rangle, |d^\pm\rangle$ modes at the Γ point evolving for a sweep of Δr. Snapshots of the corresponding displacement fields for $\Delta r = \mp 200$ nm are also shown. The in-plane displacement field is directly visualized by the deformation, whereas the out-of-plane displacement is encoded in the color scale. $d(p)$ orbitals are (anti)symmetric under rotation by 180°.
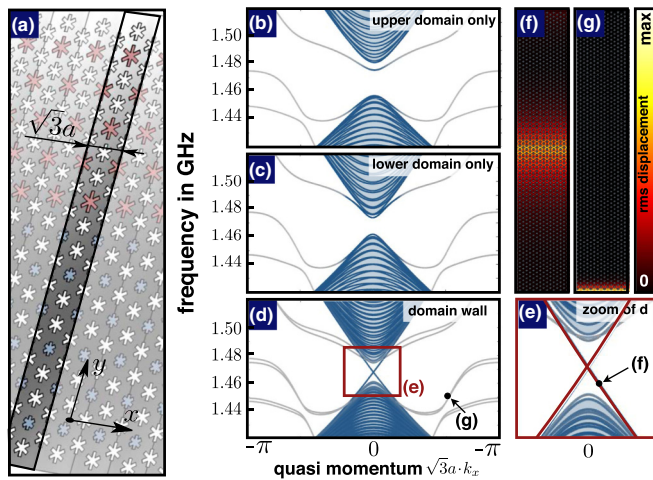
FIG. 3. FEM simulations for an infinite strip. (a) Snowflake strip configuration comprising two different domains, with the lower (upper) domain containing smaller (larger) snowflakes with $\Delta r = -200$ nm ($\Delta r = +200$ nm). The depicted strip hosts $n = 11$ resized snowflakes ($n_l = 6$ blue and $n_u = 5$ red). (b) Acoustic band structure of the blue domain only, with a system size $n = 17$. The blue shaded area indicates the strip's bulk bands, whereas the sole remaining bands are degenerate pairs of edge states localized at both boundaries of the strip. (c) Counterpart to (b) for the upper domain, essentially the strip version of Fig. 1(e). A strip comprising two domains ($\Delta r_{l/u} = \mp 200$ nm, $n_l = 18$, $n_u = 17$) has the band structure depicted in (d) and (e). In addition to the bulk modes and the edge modes at the physical boundaries (g), it reveals the two topologically protected counterpropagating modes localized at the domain wall [wave function in (f)]. For clarity, in all these band structures we just depicted the modes symmetric to the sample plane. For all FEM calculations fixed boundaries ($\mathbf{u} = \mathbf{0}$) were used at the upper and lower end of the silicon slab.

difference of π across those links) and taking into account that the p and d bands are degenerate for the original structure. Thus, the additional energy cost associated with the larger phase gradient (compared to a d orbital) across these external links exactly offsets the benefit of a reduced phase gradient on a path encircling the central snowflake when $\Delta r = 0$ (Δr is the change of radius). Obviously, stronger internal links, corresponding to a negative Δr, favor energetically the p states, leading to positive g (cf. Fig. 2).

Helical edge channels. In the presence of a domain wall where the mass g changes sign, Eq. (2) leads to helical edge states along the domain wall [35–37]. More precisely, the edge states have opposite helicity ($s \pm 1$), propagate in opposite directions with speed v, and have a penetration depth $\xi \sim |g_{\mathrm{bulk}}|/v$ [35–37]. The underlying assumption is that the mass g changes smoothly at the lattice scale. Here, we test this scenario for a sharp domain wall, solving the full elasticity equations [33]. More specifically, we consider a strip with a finite extent along y. Before investigating the effects of domain walls, we briefly discuss the strip with a spatially homogeneous mass term. Figure 3 shows the band structures of strip configurations with $\Delta r = -200$ nm [Fig. 3(b)] and $\Delta r = 200$ nm [Fig. 3(c)]. The Dirac cones are replaced by a complete bulk band gap. Moreover, localized boundary states occur due to the symmetry breaking at the sharp sample boundaries

[Fig. 3(g)], but these are not protected by any symmetry and are highly sensitive to the exact geometry of the edge.

Next, we attach both structures to each other [Fig. 3(a)] and obtain a strip geometry with a domain wall where the sign of the mass $g \propto \Delta r$ flips. The corresponding band structure is shown in Fig. 3(d). It is basically a superposition of the band structures depicted in Figs. 3(b) and 3(c). However, two new states appear that traverse the gap entirely, with a linear dispersion of opposite slope (group velocity). Moreover, there is no discernible avoided crossing between these two states, underlining the absence of backscattering expected for topological insulators due to the symmetry protection. Figure 3(f) shows the quasimomentum-resolved wave function of the right-moving state [red energy dispersion in Fig. 3(e)]. For small quasimomenta it is highly confined around the domain wall, with a typical penetration depth inversely proportional to the size of the bulk band gap (as expected from $\xi = v/g_0$).

Effects of disorder. One of the more intriguing questions is how far the helical transport is robust once the $\mathcal{C}_6$ symmetry is broken by the presence of a domain wall or by generic disorder. Here, based on simple general arguments, we identify the conditions where the resilience should be granted. Moreover, we identify two scenarios where it goes far beyond the expectations.

Any smooth perturbation can be described in the framework of an envelope function approximation by the effective Hamiltonian (2) with space-dependent parameters g and v. Thus, smooth disorder and smooth domain walls are *nonmagnetic* (they do not break the pseudo-time-reversal symmetry) and do not lead to any backscattering of topological excitations. More generally, backscattering is suppressed for any perturbation whose matrix elements between states of opposite helicity vanish for small quasimomentum transfer. One can show that this applies even to sharp defects if the defect itself has the $\mathcal{C}_6$ symmetry, e.g., a hexagonal cell where the masses of all six triangles have been changed by the same amount, or where the central snowflake hole has been left out.

Arbitrary boundaries. Next, we discuss two scenarios where the resilience of the topological transport goes well beyond the expectations. First, our FEM simulations do not show any discernible sign of backscattering for sharp, translationally invariant domain boundaries. Such a scattering would show up in the form of a minigap, i.e., an avoided crossing between the counterpropagating edge states. A similar behavior has been observed also in Refs. [29,31] for related $\mathcal{C}_6$-based photonic topological insulators. Second, inspired by this unexpected behavior, we have investigated a related scenario where the suppression of backscattering would seem at a first sight even less probable: randomly shaped domain walls. To keep the computational effort manageable, we consider a tight-binding model on the honeycomb lattice (cf. also Ref. [18]) that closely mimics our phononic crystal design [33].

As shown above, the unidirectional edge states along smooth domain walls are superpositions of the states with the same helicity s (e.g., p^+ and d^+). Figure 4 shows the energy distribution for a mechanical wave that is propagating at a randomly shaped domain wall. We excite a whole unit cell (indicated by the yellow arrow) with a $|p^-\rangle$-type mode shape, thereby launching a right-propagating mechanical wave. By calculating the linear response of each lattice site to this
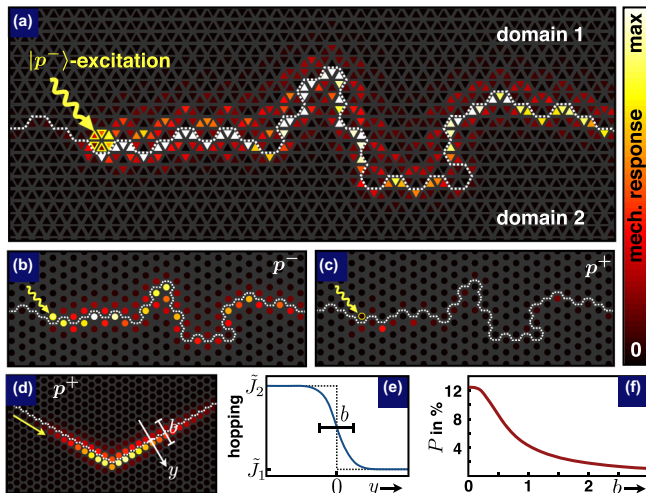
FIG. 4. Finite size sample with an arbitrarily shaped sharp domain wall, simulated using a tight-binding model. One polarization (p^-) is injected and propagates to the right, which can be identified with the wave function of Fig. 3(f). (a) Detailed representation, showing all six triangles inside each hexagonal unit cell. Color indicates the square of the mechanical wave amplitude, i.e., the energy. (b) Extracting the component of the p^- mode inside each unit cell. (c) Scattering into the other helicity (p^+) is present, but still strongly suppressed even at sharp corners. Note that in (c) we enhanced the depicted energy by a factor of 10 to make the weak scattered component visible. (d) Weak component of opposite polarization (p^+) appearing at a corner (color scale different from before). (e) Domain wall geometry (transverse to corner). (f) The total fraction of p^+ polarization decreases for a smoother domain wall.

particular excitation, we obtain the propagation probability (modulus squared of the Green's function) of the mechanical excitation. Our simulations reveal a surprisingly weak helicity flipping by the sharp randomly shaped boundaries [cf. Fig. 4(c), where the transmission of $|p^+\rangle$-type excitations is plotted]. This helicity flipping is completely suppressed when a sharp domain wall (with a sudden jump in hopping amplitudes) is replaced by even only a slightly smoothened wall [cf. Figs. 4(d)–4(f)]. Most remarkably, even for sharp boundaries there is no visible transmission to the left of the injection point [cf. Figs. 4(a)–4(d)]. In other words, the backscattering is still suppressed in spite of the randomly shaped boundaries. On the other hand, significant backscattering is introduced by moderate values (above 3%) of generic disorder (see SM [33]). A surprising resilience to sharp disorder was also observed in recent extensive FEM simulations [23] for a macroscopic acoustic metamaterial similar to the photonic design of Ref. [29].

Implementation. The snowflake phononic topological insulator proposed here is a simple modification of an existing nanoscale structure and is thus straightforward to fabricate

at any scale, down to the nanoscale. The fabrication-induced disorder observed in existing nanoscale devices is of the order of 1% [27] and will be smaller for larger scale devices. For the more complex finite structures discussed above, FEM simulations including the effects of disorder would be numerically far too expensive. However, our tight-binding calculations suggest that 1% disorder will not induce significant backscattering [33]. The remaining experimental challenge is the excitation and readout of helical mechanical waves. The most suitable approach depends on the implementation scale and ranges from mechanical, through electrical, to optomechanical (see Ref. [28]). On the nanoscale, each triangular membrane forming the snowflake lattice could host a optical cavity interacting with the edge mode via radiation pressure. In this setting, the desired mechanical waves could be induced and read out by a laser with a modulated intensity, similar to the schemes proposed in Refs. [28,38]. A helicity-selective excitation and readout of mechanical waves is possible by interfering two laser beams, one of them carrying unit orbital angular momentum [39], which produces a suitable pattern of forces. Alternatively, one could excite and read out unpolarized mechanical waves, while the helical nature of the transport could still be revealed by a beam-splitter-like setup as in Ref. [3]. We have further validated our approach performing a complete *ab initio* finite-element simulation of this setup (see SM [33]).

Outlook. The simplicity of the nanoscale design will turn the snowflake phononic topological insulator into a versatile platform for generating arbitrary phononic circuits and networks [40,41] on the chip, which may interact with hybrid quantum systems of various kinds, including embedded strain-coupled dopant-based qubits [42–44] and superconducting qubits coupled via surface-acoustic waves [45]. A qubit could emit phonons in a pseudo-spin-selective way via a triplet of electrodes applying piezoelectric strain to the snowflake triangles in a chiral fashion. These new helical phonon networks could also contain optically tunable nonreciprocal elements [46], as well as quantum-limited chiral traveling wave amplifiers of phononic signals (adapting the scheme presented in Ref. [47]).

[1] L. M. Nash, D. Kleckner, A. Read, V. Vitelli, A. M. Turner, and W. T. M. Irvine, Proc. Natl. Acad. Sci. USA **112**, 14495 (2015).

[2] R. Susstrunk and S. D. Huber, Science **349**, 47 (2015).

[3] C. He, X. Ni, H. Ge, X.-C. Sun, Y.-B. Chen, M.-H. Lu, X.-P. Liu, and Y.-F. Chen, Nat. Phys. **12**, 1124 (2016).

[4] J. Lu, C. Qiu, L. Ye, X. Fan, M. Ke, F. Zhang, and Z. Liu, Nat. Phys. **13**, 369 (2017).

[5] L. Ye, C. Qiu, J. Lu, X. Wen, Y. Shen, M. Ke, F. Zhang, and Z. Liu, Phys. Rev. B **95**, 174106 (2017).

[6] B.-Z. Xia, T.-T. Liu, G.-L. Huang, H.-Q. Dai, J.-R. Jiao, X.-G. Zang, D.-J. Yu, S.-J. Zheng, and J. Liu, Phys. Rev. B **96**, 094106 (2017).

[7] E. Prodan and C. Prodan, Phys. Rev. Lett. **103**, 248101 (2009).

[8] P. Wang, L. Lu, and K. Bertoldi, Phys. Rev. Lett. **115**, 104302 (2015).

[9] Z. Yang, F. Gao, X. Shi, X. Lin, Z. Gao, Y. Chong, and B. Zhang, Phys. Rev. Lett. **114**, 114301 (2015).

[10] T. Kariyado and Y. Hatsugai, Sci. Rep. **5**, 18107 (2015).

[11] A. B. Khanikaev, R. Fleury, S. H. Mousavi, and A. Alu, Nat. Commun. **6**, 8260 (2015).

[12] Z.-G. Chen and Y. Wu, Phys. Rev. Appl. **5**, 054021 (2016).

[13] R. Fleury, A. B. Khanikaev, and A. Alu, Nat. Commun. **7**, 11744 (2016).

[14] R. K. Pal, M. Schaeffer, and M. Ruzzene, J. Appl. Phys. **119**, 084305 (2016).

[15] J. Lu, C. Qiu, M. Ke, and Z. Liu, Phys. Rev. Lett. **116**, 093901 (2016).

[16] K. H. Matlack, M. Serra-Garcia, A. Palermo, S. D. Huber, and C. Daraio, arXiv:1612.02362.

[17] J. Mei, Z.-G. Chen, and Y. Wu, Sci. Rep. **6**, 32752 (2016).

[18] T. Kariyado and X. Hu, Sci. Rep. **7**, 16515 (2017).

[19] R. Susstrunk and S. D. Huber, Proc. Natl. Acad. Sci. USA **113**, E4767 (2016).

[20] N. P. Mitchell, L. M. Nash, D. Hexner, A. Turner, and W. T. M. Irvine, arXiv:1612.09267.

[21] H. Abbaszadeh, A. Souslov, J. Paulose, H. Schomerus, and V. Vitelli, Phys. Rev. Lett. **119**, 195502 (2017).

[22] A. Souslov, B. C. van Zuiden, D. Bartolo, and V. Vitelli, Nat. Phys. **13**, 1091 (2017).

[23] Z. Zhang, Q. Wei, Y. Cheng, T. Zhang, D. Wu, and X. Liu, Phys. Rev. Lett. **118**, 084303 (2017).

[24] R. K. Pal and M. Ruzzene, New J. Phys. **19**, 025001 (2017).

[25] V. Peano, C. Brendel, M. Schmidt, and F. Marquardt, Phys. Rev. X **5**, 031011 (2015).

[26] S. H. Mousavi, A. B. Khanikaev, and Z. Wang, Nat. Commun. **6**, 8682 (2015).

[27] A. H. Safavi-Naeini, J. T. Hill, S. Meenehan, J. Chan, S. Gröblacher, and O. Painter, Phys. Rev. Lett. **112**, 153603 (2014).

[28] C. Brendel, V. Peano, O. J. Painter, and F. Marquardt, Proc. Natl. Acad. Sci. USA **114**, E3390 (2017).

[29] L.-H. Wu and X. Hu, Phys. Rev. Lett. **114**, 223901 (2015).

[30] Y. Yang, Y. F. Xu, T. Xu, H.-X. Wang, J.-H. Jiang, X. Hu, and Z. H. Hang, arXiv:1610.07780.

[31] S. Barik, H. Miyake, W. DeGottardi, E. Waks, and M. Hafezi, New J. Phys. **18**, 113013 (2016).

[32] L. D. Landau, E. M. Lifshitz, A. M. Kosevich, and L. P. Pitaevskii, *Theory of Elasticity* (Elsevier, New York, 1986).

[33] See Supplemental Material at http://link.aps.org/supplemental/10.1103/PhysRevB.97.020102 for more details on the finite elements simulations, the tight-binding calculations as well as the derivation of the effective Hamiltonian. Also detailed there is the detection of helical transport in an interferometer like setup.

[34] B. A. Bernevig, T. L. Hughes, and S.-C. Zhang, Science **314**, 1757 (2006).

[35] M. Z. Hasan and C. L. Kane, Rev. Mod. Phys. **82**, 3045 (2010).

[36] J. K. Asboth, L. Oroszlany, and A. Palyi, *A Short Course on Topological Insulators*, Lecture Notes in Physics Vol. 919 (Springer, Berlin, 2016).

[37] R. Jackiw and C. Rebbi, Phys. Rev. D **13**, 3398 (1976).

[38] M. Schmidt, S. Kessler, V. Peano, O. Painter, and F. Marquardt, Optica **2**, 635 (2015).

[39] A. M. Yao and M. J. Padgett, Adv. Opt. Photonics **3**, 161 (2011).

[40] S. J. M. Habraken, K. Stannigel, M. D. Lukin, P. Zoller, and P. Rabl, New J. Phys. **14**, 115004 (2012).

[41] M. Schmidt, M. Ludwig, and F. Marquardt, New J. Phys. **14**, 125005 (2012).

[42] B. Golding and M. I. Dykman, arXiv:cond-mat/0309147.

[43] V. N. Smelyanskiy, A. G. Petukhov, and V. V. Osipov, Phys. Rev. B **72**, 081304 (2005).

[44] O. O. Soykal, R. Ruskov, and C. Tahan, Phys. Rev. Lett. **107**, 235502 (2011).

[45] M. V. Gustafsson, T. Aref, A. F. Kockum, M. K. Ekstrom, G. Johansson, and P. Delsing, Science **346**, 207 (2014).

[46] K. Fang, J. Luo, A. Metelmann, M. H. Matheny, F. Marquardt, A. A. Clerk, and O. Painter, Nat. Phys. **13**, 465 (2017).

[47] V. Peano, M. Houde, F. Marquardt, and A. A. Clerk, Phys. Rev. X **6**, 041026 (2016).

Correction: The first sentence of the abstract contained a word that was typeset erroneously and has been corrected.